CrossMark

On the Subparsec-scale Core Composition of FR 0 Radio Galaxies

Margot Boughelilba [ORCID] and Anita Reimer [ORCID]
Universität Innsbruck, Institut für Astro- und Teilchenphysik, A-6020 Innsbruck, Austria; margot.boughelilba@uibk.ac.at

Abstract

Although Fanaroff–Riley type 0 (FR 0) radio galaxies are known to be the most numerous jet population in the local Universe, they are much less explored than the well-established class of FR type I (FR I) and FR type II galaxies due to their intrinsic weakness. Observationally, their nuclear radio, optical, and X-ray properties are comparable to the nuclear environment of FR Is. The recent detection of two FR 0s in the high-energy band suggests that, like in FR Is, charged particles are accelerated there to energies that enable gamma-ray production. Up to now, only the lack of extended radio emission from FR 0s distinguishes them from FR Is. By comparing the spectral energy distribution of FR 0s with that of FR Is and in particular with that of M87 as a well-studied reference source of the FR I population, we find the broadband spectrum of FR 0 s exceptionally close to M87's quiet core emission. Relying on that similarity, we apply a lepto-hadronic jet-accretion flow model to FR 0s. This model is able to explain the broadband spectral energy distribution, with parameters close to particle-field equipartition and matching all observational constraints. In this framework, FR 0s are multimessenger jet sources, with a nature and highly magnetized environment similar to those of the naked quiet core of FR Is.

Unified Astronomy Thesaurus concepts: Relativistic jets (1390); Particle astrophysics (96); Fanaroff–Riley radio galaxies (526); Active galactic nuclei (16); High-energy astrophysics (739); Low-luminosity active galactic nuclei (2033); Cosmic-ray sources (328); Gamma-ray sources (633); Non-thermal radiation sources (1119)

Supporting material: data behind figure, machine-readable table

1. Introduction

Following the unified model for radio-loud active galactic nuclei (AGNs), radio galaxies have their jets misaligned with the line of sight (Urry & Padovani 1995). For that reason, radio galaxies form the dominant jetted AGN population. Because of this misalignment, the Doppler boosting enhancing the observed flux is small; hence, only a few sources have so far been detected in the gamma-ray band (see, e.g., H.E.S.S. Collaboration et al. 2018; MAGIC Collaboration et al. 2018; Ajello et al. 2022). Blazars, on the other side, with their jets pointing toward Earth, are brighter but also more rare.

Based on their extended radio morphology, radio galaxies are usually classified as either faint edge-darkened Fanaroff–Riley type I (FR I) or bright edge-brightened type II galaxies. The low-power FR Is are often linked to radiatively inefficient accretion flows, while the more powerful FR IIs are usually associated with more efficient accretion. Recently, a new type of radio galaxy has emerged, named FR type 0 (FR 0) galaxies (Baldi et al. 2018). From the radio perspective, FR 0s are similar to FR Is, except for the lack of extended emission (i.e., on a kiloparsec scale). The optical properties of FR 0s are comparable to FR Is, as they are also located in red massive early-type galaxies and are classified as low-excitation radio galaxies from a spectroscopic point of view. An X-ray study of a subsample of FR 0s (Torresi et al. 2018) showed that FR 0s have a comparable X-ray luminosity to FR Is in the 2–10 keV band, confirming the similarity of the nuclear properties of the two classes. This study also indicates low Eddington-scaled luminosities, hinting toward radiatively inefficient accretion. In

the high-energy domain, the detection of gamma rays from two of them (namely LEDA 55267 and LEDA 58287) has recently been reported (Paliya 2021; a third source is mentioned in that paper but it has been removed from the FR0CAT; see Baldi et al. 2019a). The stacking analysis of the *Fermi* Large Area Telescope (LAT) data in Paliya (2021) shows that the whole population could be considered a gamma-ray-emitting class. Previously, Grandi et al. (2016) reported the first association of one FR 0, Tol 1326-379, with a gamma-ray source in the Fermi 3FGL (for *Fermi* Gamma-ray LAT) catalog (Acero et al. 2015). The 4FGL source catalog (Abdollahi et al. 2020), however, reports no gamma-ray counterpart associated with Tol 1326-379, and it is unclear whether this FR 0 is a gamma-ray emitter or not (see, e.g., Fu et al. 2022). As of now $\gtrsim 100$ FR 0 s (FR0CAT in Baldi et al. 2018; Torresi et al. 2018) have been collected, sharing the following properties: residing at redshift $z \lesssim 0.05$, having radio sources located at maximum $2''$ from the optical center, and having a minimum FIRST flux of 5 mJy at 1.4 GHz. With these properties, FR 0s are shown to be in the order of ~ 5 times more numerous than the FR I radio galaxies in the local Universe, which makes them the dominating jet population there (Baldi & Capetti 2009, 2010).

Several hypotheses have been proposed so far to explain the lack of extended radio emission from FR 0s. Evolutionary models consider FR 0s as young sources that evolve into more extended sources. These models are, however, ruled out, due to the distribution of radio sizes in the sample (Baldi et al. 2019a). Alternatively, Garofalo et al. (2010) discussed the impact of the spin of the SMBH on the power of the associated jets. In this view, FR 0s have been proposed to be driven by a prograde, low-spin SMBH (Garofalo & Singh 2019), and most of them are not reaching spin values for which non-negligible jets are inferred.

Another approach to gain insight into the true nature of this jet population is linked to their broadband spectral energy

distribution (SED). In a recent work, Merten et al. (2021) compiled an average SED of FR 0s to collect information on their radiative environment. Here, we compare for the first time the broadband emission of FR 0s to FR Is and in particular to M87 as one of the most studied in detail archetypal FR I galaxy. M87 has been deeply studied, both in its quiet, steady state and in its flaring state. In particular, in 2017, a multiwavelength campaign focused on the quiet core emission of M87, providing constraints on the core magnetic field, the emission region, and the jet properties of M87 (EHT MWL Science Working Group et al. 2021; Event Horizon Telescope Collaboration et al. 2021).

Section 2 presents the SED data we collected and discusses the implications taken from the comparison of FR 0s and FR Is. These implications motivate a model setup for the core region of FR 0s that we describe in Section 3. Section 4 presents the results of our broadband modeling of FR 0s. Our conclusion from this study is discussed in Section 5.

2. Broadband SED

To build the broadband SED of a sample of 114 FR 0s, we collected their available data from the NASA/IPAC Extragalactic Database (NED; 2019),[1] following the method described in Merten et al. (2021). One hundred and four sources are taken from the FR0CAT (Baldi et al. 2018; note that four of the sources included in the original catalog have been removed since then. See Baldi et al. 2019a for more details). The 10 additional sources come from a sample of 19 FR 0s studied in the X-ray band (Torresi et al. 2018), among which 11 were not in the FR0CAT. From these 11 sources, we removed J004150.47-0, which is mentioned to be at the center of its cluster (Abell85, see Torresi et al. 2018), to avoid flux contamination from the cluster. For these 10 sources, additional observational data from the SSDC SED builder[2] were collected. We only use X-ray data taken with the Neil Gehrels *Swift* Observatory, *XMM*-Newton, or *Chandra* telescopes; observations from instruments with a larger angular resolution are discarded to avoid flux contamination from the sources' surroundings. Most *Chandra* data are taken from the *Chandra* Point Source Catalog 2.0.1 (Evans et al. 2020) where we use the flux_aper90 fluxes (i.e., the reported fluxes represent the background-subtracted fluxes in the modified elliptical aperture).[3] In order to have the most complete data collection available for the two individually gamma-ray detected sources, we built *Swift*-XRT spectra using the online tool.[4] For LEDA 55267, we used XSPEC (Arnaud 1996) to have a binning of 20 counts per bin to present the data. The gamma-ray data of LEDA 55267 (SDSS J153016.15+270551.0) and LEDA 58287 (SDSS J162846.13+252940.9) are taken from Paliya (2021). As mentioned in Section 1, it is unclear if Tol 1326-379 is a gamma-ray emitter since no association is reported in the 4FGL catalog (Abdollahi et al. 2020). Nevertheless, for completeness, the SED of Tol 1326-379 is included in Figure 1, with the high-energy emission butterfly representation for an integral photon flux $F_{>1\text{GeV}} = (3.1 \pm 0.8) \times 10^{-10}$ phot cm^{-2} s^{-1} and a spectral index $\Gamma = 2.78 \pm 0.14$, taken from Grandi et al. (2016). Its high-energy slope is much

steeper than that of other gamma-ray emitting FR 0s. Fu et al. (2022), however, shows that Tol 1326-379 could be associated with 4FGL J1331.0-3818, with a gamma-flux compatible with the other two gamma-ray-detected sources LEDA 55267 and LEDA 58287 although the association remains ambiguous. For these reasons, we do not consider Tol 1326-379 as a gamma-ray emitting source.

We also collected data of 216 FR I sources listed in the FRICAT (Capetti et al. 2017) in the same way. Three sources (namely FRICAT 1053+4929, FRICAT 1428+4240, and FRICAT 1518+0613) are also listed as low-luminosity BL Lac objects (Capetti & Raiteri 2015; Capetti et al. 2017), which are therefore not included in our sample.

The multiwavelength observation of M87's quiet core emission taken in 2017 (EHT MWL Science Working Group et al. 2021) are included in order to compare the broadband SED of the two classes to a typical FR I source in a quiet state. The flaring states of M87 derived by H.E.S.S in 2005 (Aharonian et al. 2006), MAGIC in 2008 (Albert et al. 2008), and VERITAS in 2007 and 2010 (Acciari et al. 2008; Aliu et al. 2012) are also used for the comparison. We use the average fitted values and uncertainties reported all together in MAGIC Collaboration et al. (2020). The list of sources used in this work is shown in the Appendix.

Figure 1 shows the resulting broadband SEDs of FR 0s compared to those of M87 and all the other FR Is, all scaled to the mean distance of FR 0s (i.e., $z \sim 0.04$). Obviously, FR 0s and FR Is show a very similar spectrum, as expected by the observation in the wave bands discussed in Section 1. The flaring-state SED of M87 (that we define as opposed to the quiet state shown in red in Figure 1 and includes the observations shown in blue) is unsurprisingly following the FR Is' trend. The lack of radio emission from FR 0s when compared to FR Is is apparent below 10^{11} Hz. What stands out in this comparison is the extreme similarity between M87's quiet core emission and the spectral behavior of FR 0s at all wavelengths.

Contrary to FR 0s, M87 has been extensively studied. Taking the above-highlighted similarity not as a chance coincidence, we are motivated to apply our knowledge deduced from M87's core observation to gain a deeper understanding—by modeling—of the FR 0s. The quiet core study of M87 infers a magnetic field strength of order (1–30 G) near the core, as well as the presence of an advection-dominated accretion flow (ADAF; Event Horizon Telescope Collaboration et al. 2021). Applying such values for the magnetic field to the simplest jet emission model, a one-zone synchrotron self-Compton (SSC) model, would result in a synchrotron-dominated SED, with a Compton dominance $(\nu_{\text{comp}}L_{\nu,\text{comp}})/(\nu_{\text{syn}}L_{\nu,\text{syn}}) \ll 1$, where ν_{syn}, ν_{comp} are the synchrotron and Compton peak frequencies, respectively, and $L_{\nu,\text{syn}}$, $L_{\nu,\text{comp}}$ are the corresponding spectral luminosities at those peak energies (see Tavecchio et al. 1998; EHT MWL Science Working Group et al. 2021). The observed high-energy gamma rays from FR 0s would then have to originate in an emission region farther down in the jet. Baldi et al. (2019b), however, disfavor the large-scale origin of the high-energy radiation from FR 0s.

A model that reproduces the radio-to-gamma-ray quiet core emission of M87 in a one-zone setup was proposed by Boughelilba et al. (2022). This model focuses on the central region of the AGN with a jet emission region of a few gravitational radii. Given the compactness of the FR 0s and the

---

[1] https://ned.ipac.caltech.edu/
[2] https://tools.ssdc.asi.it/SED/
[3] https://cxc.cfa.harvard.edu/csc/
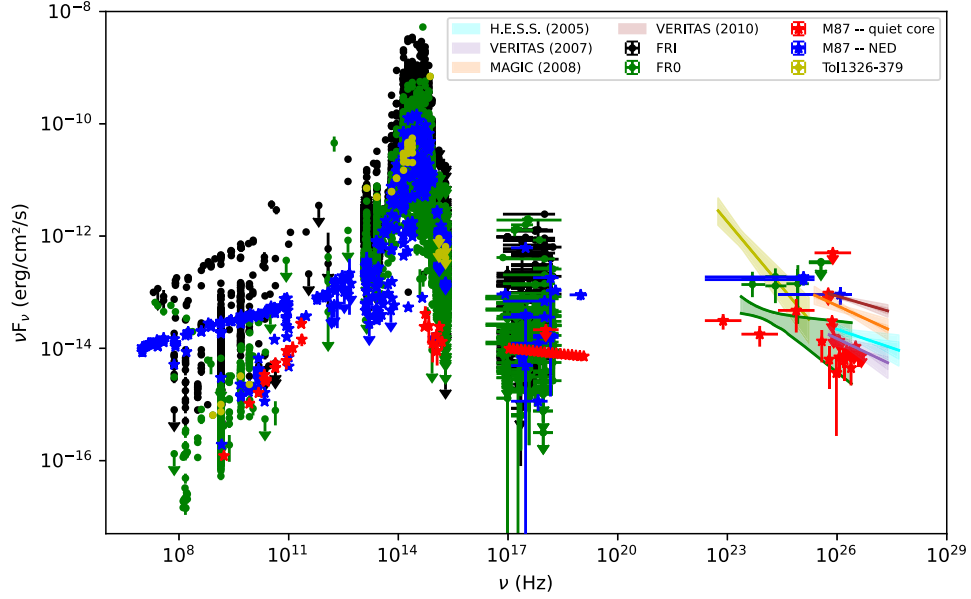[4] https://www.swift.ac.uk/user_objects/

Figure 1. Broadband SED of FR Is (black dots), FR 0 s (green dots and green butterfly on right side), M87 in its 2017 quiet state (red stars). The blue star symbols are the SED of M87 with all the observations available in the NED. The butterfly plots in the very-high-energy gamma-ray range are the power-law spectra fitted to observations of the flaring state of M87 with H.E.S.S in 2005 (cyan region), VERITAS in 2007 and 2010 (purple and brown regions, respectively), and with MAGIC in 2008 (orange region). The SED of Tol 1326-379 is shown in yellow (data points on left side), including the butterfly plot at high-energy gamma rays (shaded area on right side), using the values derived by Grandi et al. (2016). The fluxes from FR Is have been rescaled from their mean distance to the mean distance of FR 0s (i.e., from a luminosity distance $d_L \sim 1.5 \times 10^{27}$ cm to $d_L \sim 5.4 \times 10^{26}$ cm). In the same way, M87 was rescaled to the mean distance of FR 0s. The data behind this Figure is available in the .tar.gz package. The package contains three .fits table files, a Python script, and a ReadMe. Included are 114 FR 0, 216 FR I, and one M87 SED table. The script can be used to read the data files. A list of all the sources is given in the Appendix Table 3.

(The data used to create this figure are available.)

SED similarities, we explore here the same type of model for the FR 0 source class. In this model, the high-energy data are explained by the emission of protons radiating in a high magnetic field. The model also accounts for the accretion flow that is expected in such low-luminosity objects.

3. Model

3.1. Jet

In this paper, we follow the same approach as in Boughelilba et al. (2022). We consider a continuous cylindrical jet of radius R'_{em} and proper length $l' = \Gamma_j l$, with l being the observed length. We assume that the emission region contains primary relativistic electrons and protons that are isotropically and homogeneously distributed in the comoving jet frame and follow a power-law energy spectrum cutting off exponentially, such that the spectral number density $n'_{e,p}(E') \propto E'^{-p_{e,p}} e^{-E'/E'_{max,e,p}}$ cm^{-3}, for $E' \geqslant E'_{min,e,p}$ (where e, p denote the electrons or the protons, respectively).

The primary particles are continuously injected into the emission region at a rate of q_i (cm^{-3} s^{-1}), where they experience energy losses caused by various interactions. Specifically, we consider photomeson production, Bethe–Heitler pair production, inverse Compton scattering, γ–γ pair production, decay of all unstable particles, synchrotron radiation (from electrons and positrons, protons, and $\pi^\pm$, $\mu^\pm$, and $K^\pm$ before their respective decays), and particle escape at a rate of $\propto c/R'_{em}$. Positrons are treated the same way as electrons. Hence, in the following, we will use electrons to refer to the two populations irrespective of their type.

To compute the time-dependent direct emission and cascade component from the jet's particles, we use a particle and radiation transport code (see, e.g., Reimer et al. 2019) that is based on the matrix multiplication method described in Protheroe & Stanev (1993) and Protheroe & Johnson (1996). The interaction rates and secondary particles' and photons' yields are calculated by Monte Carlo event generator simulations (except for synchrotron radiation, for which they are calculated semi-analytically). These are then used to create transfer matrices, which describe how each particle spectrum will change after a given time step δt. To ensure numerical stability, we set δt equal to the smallest interaction time for any given simulation. In each time step, energy conservation is verified. The steady-state spectra are calculated by running the simulation until convergence is reached, defined here when $F_\nu(t + \delta t)/F_\nu(t) < 1 \pm 10^{-3}$.

3.2. ADAF

Low-luminosity AGNs are expected to host accretion flows in a radiatively inefficient state. This is characterized by the formation of geometrically thick, optically thin, very hot accretion flows, ADAFs (introduced by Ichimaru 1977 and Rees et al. 1982 and further developed by, e.g., Abramowicz et al. 1995; Narayan & Yi 1995). ADAFs exist only when the accretion rate is sufficiently low ($\dot{M} \lesssim 0.01\dot{M}_{Edd}$) and consist of a plasma of thermal electrons and ions, where both components may have different temperatures, T_e and T_i, respectively. Here, we investigate if and how an ADAF component would affect the global SED of FR 0s. We use the ADAF model described in Boughelilba et al. (2022) and will summarize here only the main points. In the following, we use

the normalized quantities $r = R/R_S$, with the Schwarzschild's radius $R_S = 2r_g = 2.95 \times 10^5 m_{BH}$, $m_{BH} = M_{BH}/M_\odot$, and $\dot{m} = \dot{M}/\dot{M}_{Edd} = \eta_{eff}\dot{M}c^2/L_{Edd}$, where η_{eff} is the radiation efficiency of the standard thin disk ($\eta_{eff} \approx 0.1$) and the Eddington luminosity $L_{Edd} \simeq 1.3 \times 10^{47} m_{BH,9}$ erg s^{-1}. We obtain the electron temperature by varying T_e using a bisection method to solve the balance equation $q^{e+} = q^{e-}$ for each radius. Here q^{e+} is the electrons' heating rate, and q^{e-} is their cooling rate. The cooling mechanisms that we consider are synchrotron radiation, bremsstrahlung, and Comptonization of the two previous components. The heating mechanisms consist of Coulomb collision between ions and electrons and viscous energy dissipation. We make use of the one-zone, height-integrated, self-similar solutions of the slim disk equations derived by Narayan & Yi (1995) to describe the hot plasma. These solutions are appropriate only after the sonic point (Narayan et al. 1997), corresponding to $\gtrsim 2$–$5 r_g$. The quantities governing the accretion flow depend on the plasma parameter β, which is the ratio between the gas and the total pressure (i.e., the sum of the magnetic and gas pressure), on the viscosity α, and on the heating fraction δ_e, which represents the fraction of viscous energy directly transmitted to the electrons of the plasma.

Furthermore, we take $\dot{m}$ of the form $\dot{m} = \dot{m}_{out}(r/r_{out})^s$, where r_{out} is the outer radius of the ADAF and is associated with an accretion rate $\dot{m}_{out}$, and s is a mass-loss parameter (introduced by Blandford & Begelman 1999) that is used to include the presence of outflows or winds from the ADAF. Upon obtaining the electron temperature, the emitted spectrum from the ADAF is computed, integrating over the radius of the ADAF.

4. Results

Motivated by the similarity of the broadband SED of FR 0s to the one of M87's quiet core, we explore parameter sets for the modeling of the FR 0s' emission that are close to the M87 core model of Boughelilba et al. (2022). For the ADAF, we use the same viscosity $\alpha = 0.1$ and heating fraction $\delta_e = 5 \times 10^{-3}$. We fix the value of the plasma β parameter to $\beta = 0.99$, which leads to a magnetic field strength in the central region of the ADAF to be of the order of the estimated jet's core magnetic field strength. Lower values of β would imply unreasonably large magnetic field strengths. For the radial dependence of the accretion rate, parameterized by the index s, we explored values from 0.1 to 1 (the larger s is, the more powerful the outflow). Fixing s to $s = 0.1$ appears to be a reasonable trade-off between the expected lower power of the jets (compared to M87's jet, where s is set to $s = 0.4$) and the radiative flux resulting from such ADAF configurations. We fix $r_{out} = 5 \times 10^3$, which is a typical value for an ADAF's extension and is well below the size of FR 0s, in the absence of other constraints.

For a black hole mass range of $10^{7.4} \leqslant M_{BH}/M_\odot \leqslant 10^9$ (Baldi et al. 2018; with a mean value of $M_{BH} \approx 10^{8.4} M_\odot$) for the FR 0 source class, one expects a lower ADAF X-ray luminosity than for the FR Is possessing black holes with a mass range of $10^8 \leqslant M_{BH}/M_\odot \leqslant 10^{9.5}$ (and with a mean value of $M_{BH} \approx 10^{8.55} M_\odot$).

For adjusting the accretion rate in order to match the observations, we follow a step-by-step procedure. First, the accretion rate is set to the highest allowed value (for a given α, β, and M_{BH}; Narayan & Yi 1995). Then, we compute the associated magnetic field in the central region (namely where

Table 1
Jet Parameters Used in the Case $B = 25$ G

	LEDA 55267	LEDA 58287	Subthreshold Sample
R'_{em} (cm)	4.0×10^{15}	4.0×10^{15}	4.0×10^{15}
$n'_{inj,e}$ (cm^{-3} s^{-1})	1.4×10^{-2}	1.6×10^{-3}	4.8×10^{-4}
$n'_{inj,p}$ (cm^{-3} s^{-1})	3.9×10^{-6}	3.7×10^{-6}	1.8×10^{-6}
$E'_{min,e}$ (MeV)	0.5	0.5	0.5
$E'_{max,e}$ (MeV)	1.2×10^4	8.0×10^3	1.5×10^4
$E'_{min,p}$ (GeV)	1.0	1.0	1.0
$E'_{max,p}$ (GeV)	3.0×10^9	5.5×10^9	2.0×10^9
$p_e = p_p$	1.7	1.7	1.7
$u'_{part,ss}/u'_B$	2.1×10^{-1}	9.7×10^{-2}	3.5×10^{-2}
$L'_{jet,ss}$ (erg s^{-1})	3.6×10^{43}	3.3×10^{43}	3.1×10^{43}

Note. The size of the emission region is R'_{em}, $n'_{inj,e(p)}$ is the electron (proton, $n'_{inj,p}$) number density injection rate, and both types of particles are injected with spectral indices $p_{e,p} = 1.7$, following the spectral shape described in Section 3.1. $u'_{part,ss}/u'_B$ and $L'_{jet,ss}$ represent the energy density ratio and jet power respectively, after the steady state is reached in the emission region.

Table 2
Same as in Table 1 for the Case $B = 25$ G

	LEDA 55267	LEDA 58287	Subthreshold sample
R'_{em} (cm)	1.2×10^{15}	1.2×10^{15}	1.2×10^{15}
$n'_{inj,e}$ (cm^{-3} s^{-1})	4.2×10^{-1}	3.2×10^{-2}	1.9×10^{-2}
$n'_{inj,p}$ (cm^{-3} s^{-1})	1.3×10^{-4}	1.9×10^{-4}	8.2×10^{-5}
$E'_{min,e}$ (MeV)	0.5	0.5	0.5
$E'_{max,e}$ (MeV)	8.0×10^3	8.0×10^3	8.0×10^3
$E'_{min,p}$ (GeV)	1.0	1.0	1.0
$E'_{max,p}$ (GeV)	3.0×10^9	4.0×10^9	1.5×10^9
$p_e = p_p$	1.7	1.7	1.7
$u'_{part,ss}/u'_B$	4.8×10^{-1}	2.9×10^{-1}	1×10^{-1}
$L'_{jet,ss}$ (erg s^{-1})	1.5×10^{43}	1.3×10^{43}	1.1×10^{43}

$R \leqslant R'_{em}$). If the magnetic field strength in the ADAF there exceeds the value of the jet's core magnetic field, we decrease the accretion rate accordingly to reach this value. The accretion rate can be further reduced if needed to match the observations. The ADAF spectrum is then calculated with the method described above. We do so for the two gamma-ray detected sources, as well as for the 23 other sources where X-ray data are available. The resulting SED is a combination of the ADAF component, the jet component, and the host galaxy's modified blackbody.

FR 0s' jets are expected to be less powerful than FR Is' and only mildly relativistic (Giovannini et al. 2023). Therefore, we explored parameters similar to those used to model M87 (Boughelilba et al. 2022), except with a lower value for the average relative jet bulk velocity β_j, namely $\beta_j = 0.55$, and a jet inclination with respect to the line of sight of 20°. We consider a magnetic field strength in the range $\sim$10–50 G, primary particle spectral indices of 1.7–2.3 and an emission region of a few to hundreds of gravitational radii in size. Lower values for the magnetic field strength imply X-ray fluxes that do not reach the observed level: for the same ADAF parameters, lowering the magnetic field strength implies decreasing the accretion rate, which results in correspondingly lower X-ray luminosities. Satisfactory results are obtained when using magnetic field strengths in the range 25–50 G. The emission region's size
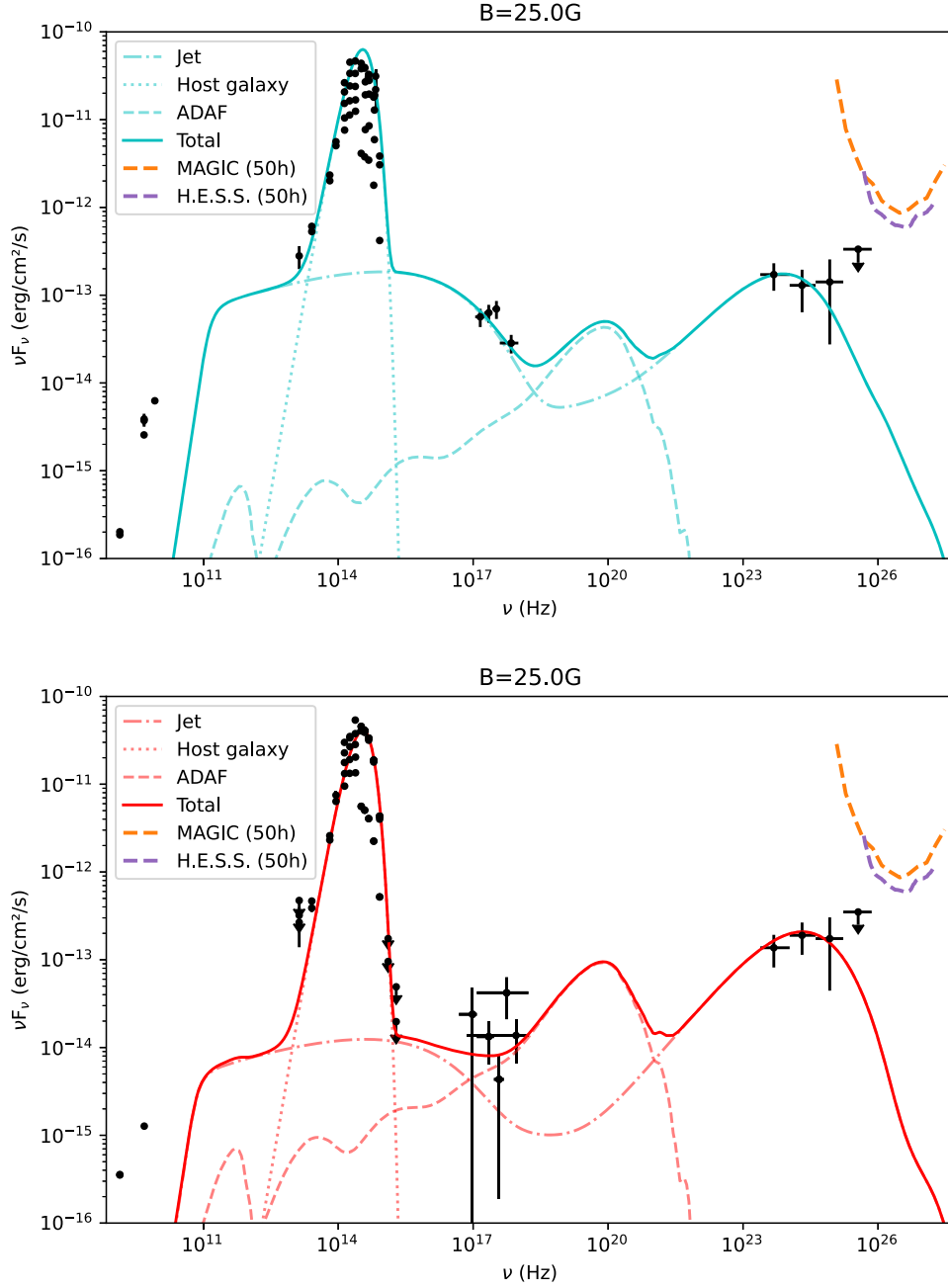
Figure 2. SEDs of the two gamma-ray sources, for a magnetic field strength of 25G in the jet. Top: SED of LEDA 55267. The dotted line is the modified blackbody modeling the host galaxy emission, the dashed line is the emission coming from the ADAF, the dashed–dotted line is the total jet's emission, and the solid line represents the total emission of the source and is the sum of the three components. The differential fluxes sensitivities for 50 hr of observation with MAGIC (Aleksić et al. 2016) and H.E.S.S (Holler et al. 2015) are shown with the orange and purple dashed lines, respectively. Bottom: same for LEDA 58287.

varies from $R'_{\mathrm{em}} = 4 \times 10^{15}$ cm for $B = 25$ G to $R'_{\mathrm{em}} = 1.2 \times 10^{15}$ cm for $B = 50$ G in order not to overshoot the available jet power (predicted in the range $10^{42.5}$–$10^{43.5}$ erg s^{-1} for FR 0s (Heckman & Best 2014; Merten et al. 2021).

To allow the jet emission to reach the X-ray energies and corresponding flux levels, a hard slope is preferred, and better fits are achieved with an electron spectral index of $p_{\mathrm{e}} = 1.7$. The proton spectral index is mainly constrained by the resulting jet power. For that reason, we keep models with $p_{\mathrm{p}} = 1.7$. The maximum proton energy varies from $E'_{\mathrm{max},p} = 10^9$ GeV to $E'_{\mathrm{max},p} = 5.5 \times 10^9$ GeV. We model the two gamma-ray-detected sources individually; for the subthreshold sample we aim at an average description of the population. The injection

parameters and some resulting quantities for the different models are given in Tables 1 and 2.

Our best-fit accretion rate values depend on the magnetic field strength present in this region. We find values for the accretion rate at the outer boundary of the flow of $\dot{m}(r = r_{\mathrm{out}}) \sim 6 \times 10^{-4} - 2 \times 10^{-3}$ when the jet's magnetic field strength is $B = 25$ G whereas $\dot{m}(r = r_{\mathrm{out}}) \sim 1 \times 10^{-3} - 4 \times 10^{-3}$ for $B = 50$ G.

In Figure 2, we present the SEDs and their model representations of LEDA 55267 and LEDA 58287 from top to bottom, respectively, for a jet magnetic field strength of 25G. As described above, the 23 subthreshold sources with X-ray data possess a modeled ADAF and a jet. All the 112
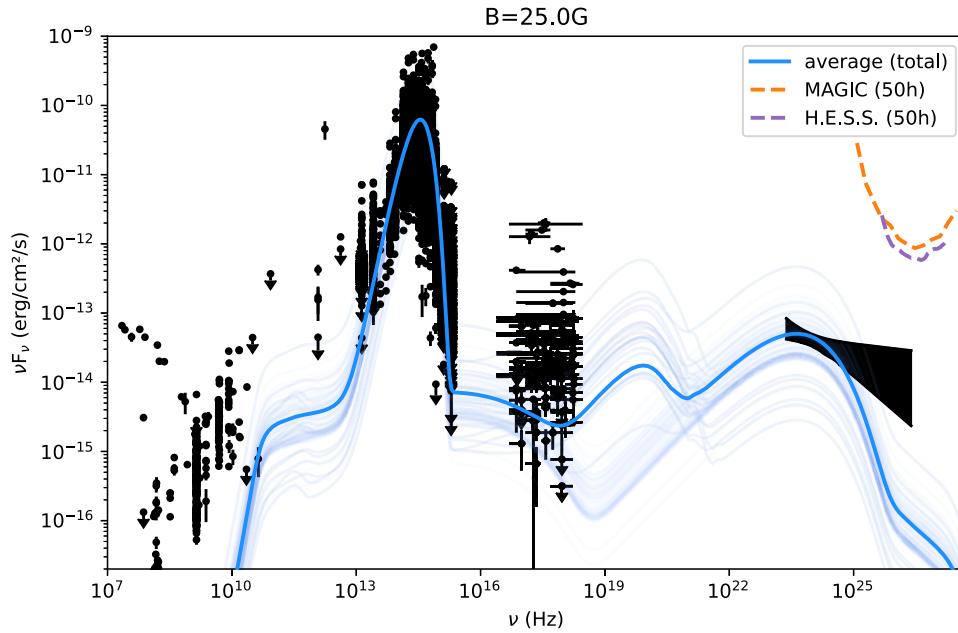
Figure 3. SEDs of the 112 sources that are not individually detected in the gamma-ray band for a magnetic field strength of 25G in the jet. The faint blue lines are the individual fluxes of the 112 sources (see Section 4 for details), and the solid blue line is the average of the 112 models. The differential flux sensitivities for 50 hr of observation with MAGIC (Aleksić et al. 2016) and, H.E.S.S (Holler et al. 2015) are shown with the orange and purple dashed lines, respectively.

subthreshold sources are modeled with the same jet parameters. For each source, the observed flux is calculated from the emitted luminosity, given their respective distance to Earth. The corresponding SEDs are displayed in Figure 3 in faint blue. The average SED of the 112 FR 0s is shown as a solid plain blue line there. The same is shown in Figures 4 (for LEDA 55267 and LEDA 58287) and 5 (for the subthreshold sample) for a jet magnetic field strength of 50G. The TeV flux predicted by our models lies far below the sensitivity curves of the current Cherenkov telescopes.[5]

We predict a strong MeV contribution from the ADAF to the overall sources' SED (even if slightly less important in the case of $B = 25$ G). This component could be probed by future MeV gamma-ray instruments like e-ASTROGAM (De Angelis et al. 2017) or the All-sky Medium Energy Gamma-ray Observatory eXplorer (Caputo et al. 2022).

The steady-state jet power is estimated by $L'_{\text{jet,ss}} = \pi R'^2_{\text{em}} \Gamma^2_{\text{j}} \beta_{\text{j}} c \sum_i u'_i$, where u'_i is the energy density of radiation, electrons, protons ($u'_{\text{part,ss}}$), and magnetic field (u'_{B}), respectively. We assume a neutral jet and hence account for cold protons to balance the electrical charge. In the case of $B = 25$ G, we find the jet to be slightly magnetically dominated, i.e., $u'_{\text{part,ss}}/u'_{\text{B}} \approx 3.5 \times 10^{-2} - 0.1$. For $B = 50$ G, the jet composition is very close to equipartition, i.e., $u'_{\text{part,ss}}/u'_{\text{B}} \approx 0.1-0.5$. The resulting jet power is in the range $(1.1-1.5) \times 10^{43}$ erg s^{-1} for $B = 50$ G and $(3.0-3.6) \times 10^{43}$ erg s^{-1} for $B = 25$ G. Our calculated neutrino output of the models predicts neutrino fluxes far below the current instruments' sensitivities (peak fluxes lie at $\lesssim 10^{-13}$ GeV cm^{-2} s^{-1} with a peak energy of $E_{\text{peak}} \sim 10^{17-18}$ eV).

5. Conclusion

Aiming to gain a deeper understanding of the dominating jet population in the local Universe, FR 0 radio galaxies, we compared these to the more extended but comprehensively studied FR Is. We found that the broadband SED of FR 0s is extremely similar to the archetypal FR I, M87, during its quiet steady state (described in detail in EHT MWL Science Working Group et al. 2021). The similarity goes from the core radio emission to the X-ray band and up to gamma rays for two individual sources detected in the high-energy band.

This motivates us to consider an environment described by physical parameter values that is comparable to M87's quiet core. To test this, we applied a one-zone lepto-hadronic jet model, combined with the emission of an ADAF to the FR 0 population. Alternatively, two-zone models, like a spine-sheath jet structure, are not rejected. Indeed, recently, Baldi et al. (2021), Cheng et al. (2021), and Giovannini et al. (2023) showed that FR 0s have a smaller jet-to-counterjet ratio than FR Is on a parsec scale. This suggests that FR 0s' jets are mildly, or even not, relativistic, which can also be interpreted as the presence of a faint relativistic spine and a dominant slow sheath structure in the jet. In this framework, if FR 0s' jets are seen at a large viewing angle, as indicated by observations, mainly the sheath emission would be observed, and our results can be interpreted as the emission from this zone at the first order. In the one-zone model context, we found that a compact subparsec-scale jet-flow emission region (from a few to a thousand gravitational radii for the jet to $5 \times 10^3 r_g$ for the ADAF, leading to a global region size of $\sim 6 \times 10^{-3} - 0.3$ pc) is able to explain the nuclear multiwavelength SED of FR 0s, provided that a magnetic field strength of 25–50 G is reached in the core region. As reviewed by Baldi & Ranieri (2023), lower values of the magnetic field strength are expected to prevent the formation of large-scale jets and explain the lack of extended emission in FR 0 s. N. Khatiya et al. (2023, in preparation) explore broadband modeling scenarios with such low field

---

[5] The MAGIC differential sensitivity is available in machine-readable format at https://magic.mpp.mpg.de/newcomers/magic-team/technical-implementation0/, and the H.E.S.S curve is adapted from Holler et al. (2015). See https://www.cta-observatory.org/science/ctao-performance/.
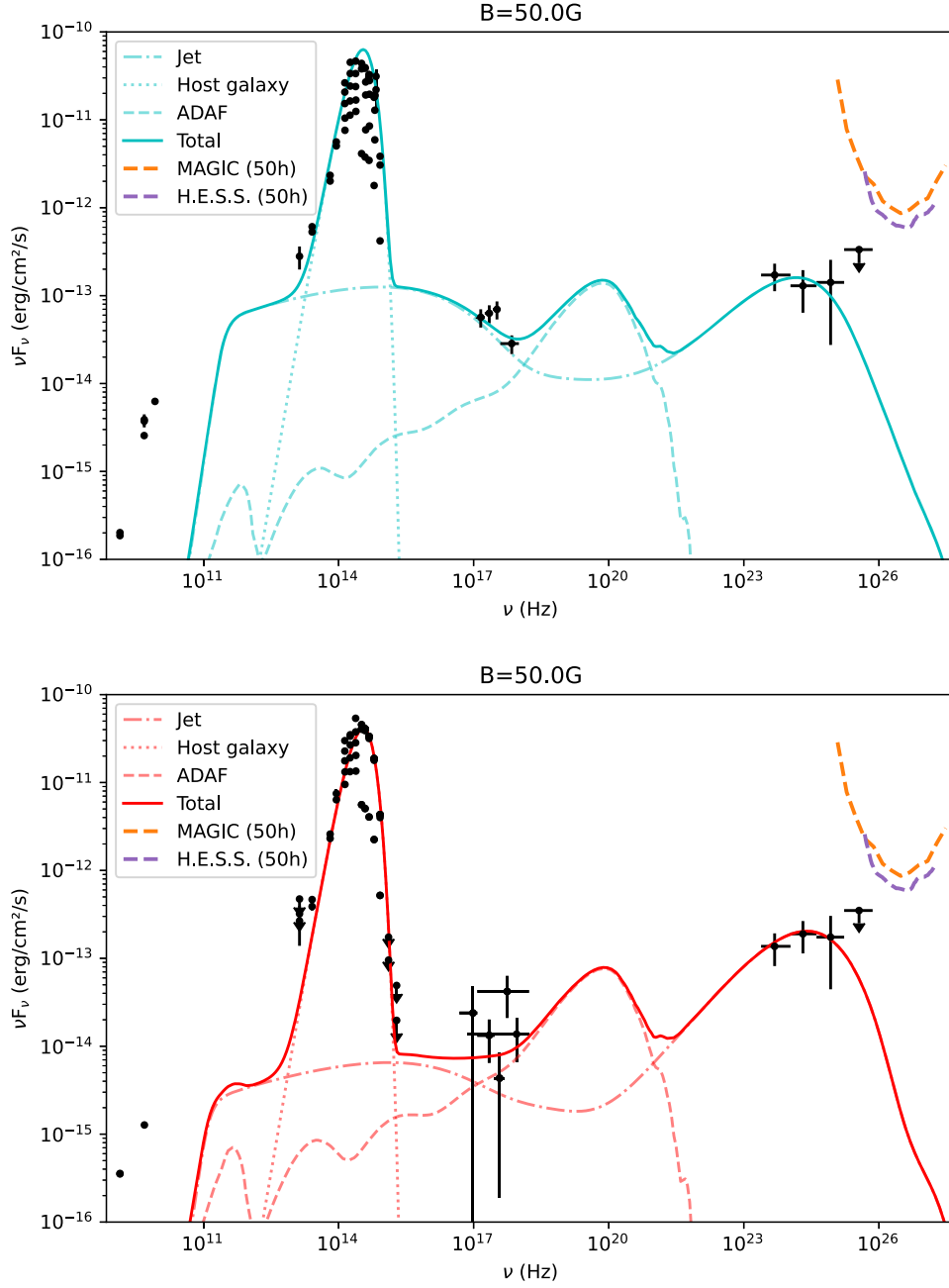
Figure 4. Same as Figure 2 but for $B = 50$G.

strengths, where the jet's composition is strongly particle dominated, and leptons can account for the high-energy observations.
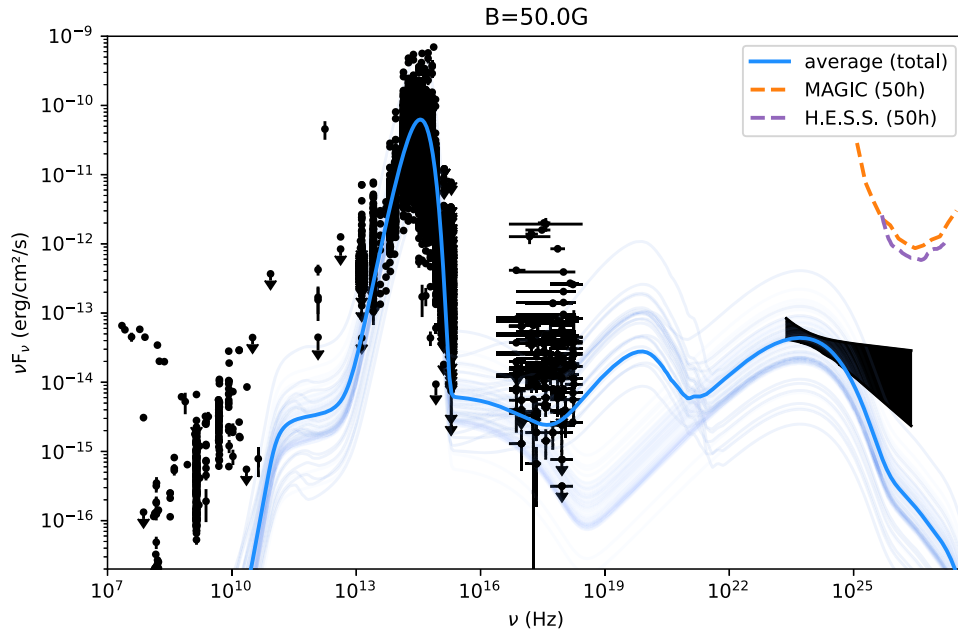
In this model, the jet of FR 0s is mildly relativistic, with a velocity $\beta_j c = 0.55\,c$, which is consistent with the value obtained by Giovannini et al. (2023) when observing the core of FR 0s in comparison to FR Is. The jet contributes mainly to the radio and gamma-ray band. The optical observations are dominated by the host galaxy. The jet and the ADAF both contribute to the X-ray band, predicting a strong ADAF-dominated MeV flux component.

As protons are, in this framework, accelerated up to $\sim 6 \times 10^{18}$ eV, FR 0s are multimessenger sources and could contribute to the cosmic-ray flux up to the ankle ($E' \approx 10^{18}$ eV; see also Merten et al. 2021; Lundquist et al. 2022).

In this view, we find that FR 0s, given their observed nuclear properties and their broadband SED, are of a similar nature as that of the naked quiet core of FR Is, whose best-studied representation is the quiet core of M87.

Figure 5. Same as Figure 3 but for $B = 50$G.

Software: This work benefited from the following software: NumPy (van der Walt et al. 2011), Matplotlib (Hunter 2007), pandas (Wes McKinney 2010; Jeff 2022), jupyter notebooks (Pèrez & Granger 2007).

Appendix

The list of sources used in this paper is shown in Table 3. It contains 114 FR 0 and 216 FR I objects.

Table 3
The FR 0 and FR 1 Source List

Name
FR 0
SDSS J010101.12-002444.4
SDSS J010852.48-003919.4
SDSS J011204.61-001442.4
FR I
SDSS J002900.90-011341.7
SDSS J003930.52-103218.6
SDSS J004148.22-091703.1

Note.

(This table is available in its entirety in machine-readable form.)

ORCID iDs

Margot Boughelilba ● https://orcid.org/0000-0003-1046-1647
Anita Reimer ● https://orcid.org/0000-0001-8604-7077

References

Abdollahi, S., Acero, F., Ackermann, M., et al. 2020, ApJS, 247, 33
Abramowicz, M. A., Chen, X., Kato, S., Lasota, J.-P., & Regev, O. 1995, ApJL, 438, L37
Acciari, V. A., Beilicke, M., Blaylock, G., et al. 2008, ApJ, 679, 397
Acero, F., Ackermann, M., Ajello, M., et al. 2015, ApJS, 218, 23
Aharonian, F., Akhperjanian, A. G., Bazer-Bachi, A. R., et al. 2006, Sci, 314, 1424

Ajello, M., Baldini, L., Ballet, J., et al. 2022, ApJS, 263, 24
Albert, J., Aliu, E., Anderhub, H., et al. 2008, ApJL, 685, L23
Aleksić, J., Ansoldi, S., Antonelli, L. A., et al. 2016, APh, 72, 76
Aliu, E., Arlen, T., Aune, T., et al. 2012, ApJ, 746, 141
Arnaud, K. A. 1996, in ASP Conf. Ser. 101, Astronomical Data Analysis Software and Systems V, ed. G. H. Jacoby & J. Barnes (San Francisco, CA: ASP), 17
Baldi, Ranieri D. 2023, A&ARv, 31, 3
Baldi, R. D., & Capetti, A. 2009, A&A, 508, 603
Baldi, R. D., & Capetti, A. 2010, A&A, 519, A48
Baldi, R. D., Capetti, A., & Giovannini, G. 2019a, MNRAS, 482, 2294
Baldi, R. D., Torresi, E., Migliori, G., & Balmaverde, B. 2019b, Galax, 7, 76
Baldi, R. D., Capetti, A., & Massaro, F. 2018, A&A, 609, A1
Baldi, R. D., Giovannini, G., & Capetti, A. 2021, Galax, 9, 106
Blandford, R. D., & Begelman, M. C. 1999, MNRAS, 303, L1
Boughelilba, M., Reimer, A., & Merten, L. 2022, ApJ, 938, 79
Capetti, A., Massaro, F., & Baldi, R. D. 2017, A&A, 598, A49
Capetti, A., & Raiteri, C. M. 2015, A&A, 580, A73
Caputo, Regina, Ajello, Marco, Kierans, Carolyn A., et al. 2022, JATIS, 8, 044003
Cheng, X., An, T., Sohn, B. W., Hong, X., & Wang, A. 2021, MNRAS, 506, 1609
De Angelis, A., Tatischeff, V., Tavani, M., et al. 2017, ExA, 44, 25
Evans, I. N., Primini, F. A., Miller, J. B., et al. 2020, AAS Meeting Abstracts, 235, 154.05
Event Horizon Telescope Collaboration, Akiyama, K., Algaba, J. C., et al. 2021, ApJL, 910, L13
EHT MWL Science Working Group, Algaba, J. C., Anczarski, J., et al. 2021, ApJL, 911, L11
Fu, W.-J., Zhang, H.-M., Zhang, J., et al. 2022, RAA, 22, 035005
Garofalo, D., Evans, D. A., & Sambruna, R. M. 2010, MNRAS, 406, 975
Garofalo, D., & Singh, C. B. 2019, ApJ, 871, 259
Giovannini, G., Baldi, R. D., Capetti, A., Giroletti, M., & Lico, R. 2023, A&A, 672, A104
Grandi, P., Capetti, A., & Baldi, R. D. 2016, MNRAS, 457, 2
Heckman, T. M., & Best, P. N. 2014, ARA&A, 52, 589
Holler, M., de Naurois, M., Zaborov, D., Balzer, A., & Chalmé-Calvet, R. 2015, ICRC, 34, 980
Hunter, J. D. 2007, CSE, 9, 90
H. E. S. S. Collaboration, Abdalla, H., Abramowski, A., et al. 2018, A&A, 619, A71
Ichimaru, S. 1977, ApJ, 214, 840
Jeff, R. 2022, pandas-dev/pandas: Pandas, v1.4.2, Zenodo, doi:10.5281/zenodo.6408044
Lundquist, J. P., Merten, L., Vorobiov, S., et al. 2022, ICRC, 37, 989
Merten, L., Boughelilba, M., Reimer, A., et al. 2021, APh, 128, 102564

MAGIC Collaboration, Acciari, V. A., Ansoldi, S., et al. 2020, MNRAS, 492, 5354

MAGIC Collaboration, Ansoldi, S., Antonelli, L. A., et al. 2018, A&A, 617, A91

Narayan, R., Kato, S., & Honma, F. 1997, ApJ, 476, 49

Narayan, R., & Yi, I. 1995, ApJ, 452, 710

NASA/IPAC Extragalactic Database (NED) 2019, NASA/IPAC Extragalactic Database (NED), IPAC, doi:10.26132/NED1

Paliya, V. S. 2021, ApJL, 918, L39

Pèrez, F., & Granger, B. E. 2007, CSE, 9, 21

Protheroe, R. J., & Johnson, P. A. 1996, APh, 4, 253

Protheroe, R. J., & Stanev, T. 1993, MNRAS, 264, 191

Rees, M. J., Begelman, M. C., Blandford, R. D., & Phinney, E. S. 1982, Natur, 295, 17

Reimer, A., Böttcher, M., & Buson, S. 2019, ApJ, 881, 46

Tavecchio, F., Maraschi, L., & Ghisellini, G. 1998, ApJ, 509, 608

Torresi, E., Grandi, P., Capetti, A., Baldi, R. D., & Giovannini, G. 2018, MNRAS, 476, 5535

Urry, C. M., & Padovani, P. 1995, PASP, 107, 803

van der Walt, S., Colbert, C. S., & Varoquaux, G. 2011, CSE, 13, 22

Wes McKinney 2010, in Proc. of the 9th Python in Science Conf., ed. S. van der Walt & J. Millman, 56